

Electronic Supplementary Information

Multifunctional sound-absorbing and mechanical metamaterials via a decoupled mechanism design approach

Zhendong Li ^{a,b}, Xinwei Li ^b, Zhonggang Wang ^{a,*}, Wei Zhai ^{b,*}

^a School of Traffic & Transportation Engineering, Central South University, Changsha 410075, Hunan, China

^b Department of Mechanical Engineering, National University of Singapore, Singapore 117575, Singapore

* Corresponding author

E-mail address: wangzg@csu.edu.cn

E-mail address: mpezwei@nus.edu.sg

Section S1. Material design: principle, specimen, and geometry

Besides the target of absorbing audible sound in low-frequency, broadband absorption is significant in practical applications^{1,2}. Herein Fig. S1(a)-(b) demonstrates its physical properties and our design recipe for achieving the broadband absorption, respectively.

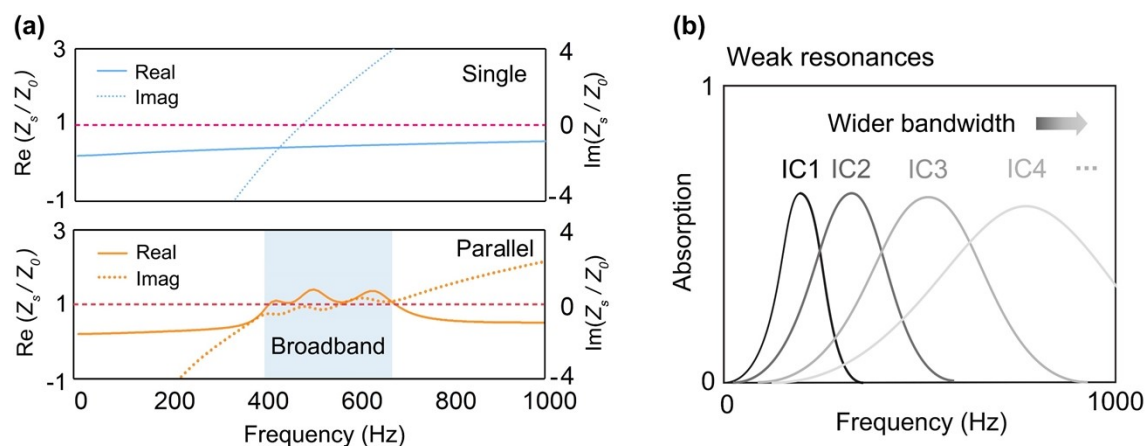


Fig. S1. Impedance comparison and design recipe. (a) Compared relative acoustic impedance of a single and a parallel circuit. (b) Schematic of designing weak absorption for each IC.

Table S1. Geometric parameters of the systems in Fig. S1(a) (Unit: mm).

Parameters	L	t_{plate}	d_i	σ_i	D
Single circuit	12.00	2.00	1.30	0.92%	48.00

			1.30	0.92%	
Parallel circuit	12.00	2.00	1.05	1.20%	48.00
			0.90	1.77%	
			0.80	2.79%	

The specimen in Fig. 2(b) in the main text is prepared for compression test. It consists of two macroscopic acoustic units, i.e., eight ICs. The side length L_c of the specimen is 12.00 mm. The dimensional size in x , y , and z direction is characterized by C_x , C_y and C_z , respectively. So, corresponding values are: $C_x = 48.00$ mm, $C_y = 24.00$ mm, and $C_z = 50.00$ mm. Table S2 shows the variables of re-entrant struts of the specimen. The thickness of struts is taken into account in the dimensional value of L_r and H_r . Owing to the unique configuration, only one complete re-entrant cell in the plane direction in the cavity is constructed. H_r is 9.00 mm for ensuring complete cells along z direction, and herein the cell number is 6 in z direction.

Table S2. Geometries for re-entrant struts (Unit: mm).

Parameters	L_r	H_r	θ_r	t_r	D
Value	6.86	9.00	81°	1.00	48.00

Sound-absorbing specimens have different dimensional sizes compared with the compressive samples owing to the specific requirements of impedance tube. Two absorbers with varying side length L_c are designed for validating the accuracy of numerical models. Sample 2 has the same mechanical units as Sample 1 (Table S2) with the spared parts are cut off to ensure L_c equaling to 10 mm. For an overall excellent absorption spectrum, their geometric parameters (Table S3) are tuned for the weak resonances by the theoretical model. The acoustic resistance and reactance are both considered for the proper absorption peak values and peak frequencies.

Table S3. The designed geometries for sound-absorbing samples (Unit: mm).

Parameters	L_c	t_{plate}	d_i	σ_i	D
Sample 1	12.00	2.00	1.40	1.07%	48.00
			1.10	1.32%	
			0.90	1.77%	
			0.80	2.79%	
Sample 2	10.00	2.00	1.20	1.13%	48.00

	1.00	1.57%
	1.00	2.36%
	1.00	3.93%

Representative microscopic images of the pores of samples are shown below. From Fig. S2(a) and (b), notable fabrication defects are observed for these samples, including irregular shape rather than circles, roughness surrounding the pores, and narrowing diameter from bottom to top. From the cross-sectional view in Fig. S2(c), we found that only the first top layer, that is, substrate layer, has smaller diameter, while all other layers possess the wide diameters. By measuring from bottom view, there is a certain degree of geometries deviations between the as-printed and the theoretical design, as summarized in Table S4.

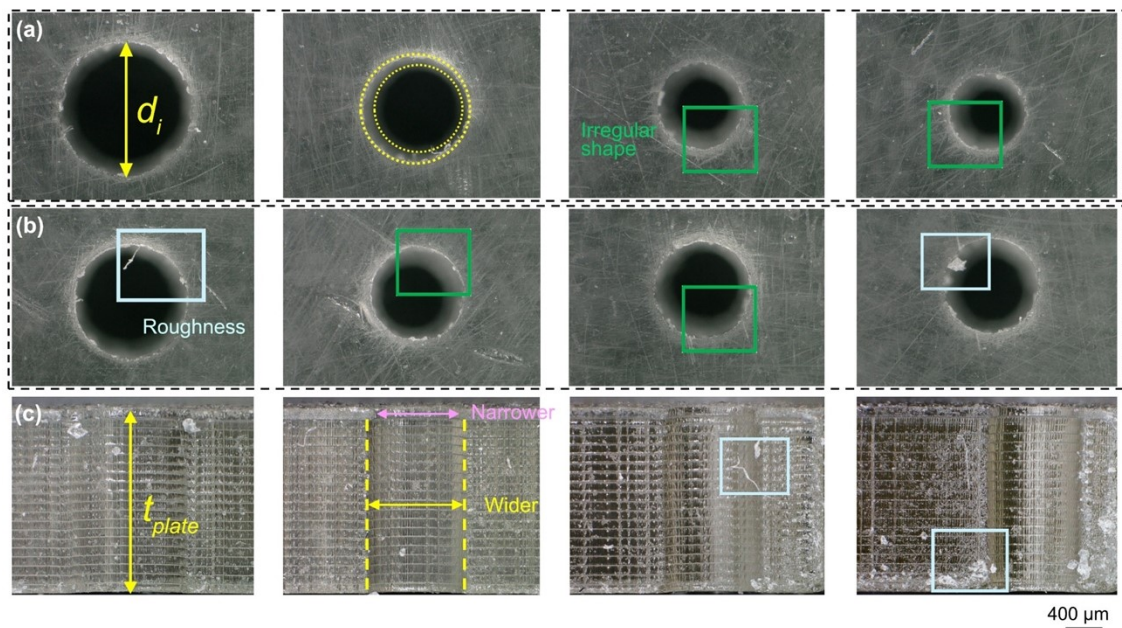


Fig. S2. Representative microscopic images of the pores of (a) Sample 1 and (b) Sample 2 from bottom view, and (c) cross-sectional view of the pores of Sample 1. Scalebar corresponds to 400 μm for all the images.

Table S4. The designed and experimentally measured dimensions of pore sizes (Unit: μm).

	Design	1400	1100	900	800
Sample 1	As-printed	1413 \pm 5	1115 \pm 12	917 \pm 8	822 \pm 11
	Design	1200	1100	1100	1100
Sample 2	As-printed	1209 \pm 5	1015 \pm 7	1015 \pm 13	1016 \pm 12

The impedance tube system is shown in Fig. S3(a). To meet the requirements of dimensions, the computed-aided models are obtained via cutting the cylinder out from 6×6 macroscopic units. The calculated and simulated absorption of Sample 1 are shown in Fig. S3(b). They agree well in general trend and main working frequency regime. The deviation is discussed later.

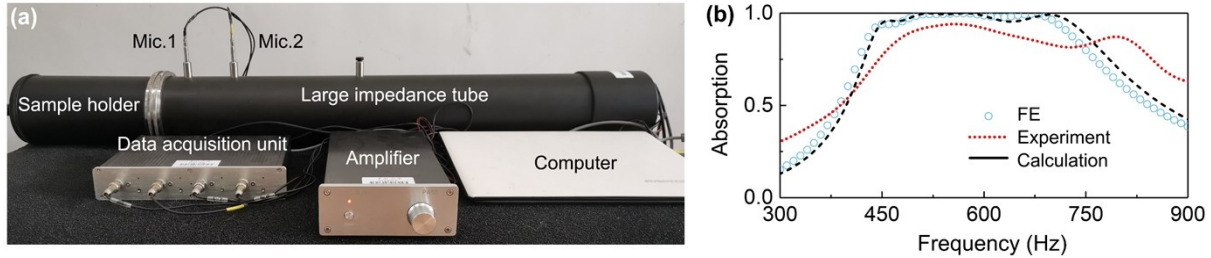


Fig. S3. Experimental set-up and measured absorption. (a) The set-up for measuring low-frequency sound range (64-1600 Hz), requiring the specimen to be a cylinder with diameter of 100 mm to adapt the large tube. (b) Sound absorption performance of Sample 1.

Based on Table S4, the experimentally corrected dimensions are then input into the calculations of Sample 1 and Sample 2 with the absorption coefficients plot in Figure S4(a) and (b), respectively. There are still some derivations exist. Actually, the slight frequency shift is commonly seen for heterogeneous absorbers^{3,4} whose tiny deviation of diameters may lead to big change in measured absorption. One reason is that not all the imperfections of the samples have been considered for correction. For example, the roughness and irregularity of pores shown in Fig. S2, and other potential defects in walls or plates. Another reason may be attributed to the close individual absorption peaks, which can result in the merging effect of peaks, and thus the measured spectra exhibit less peaks.^{4,5}

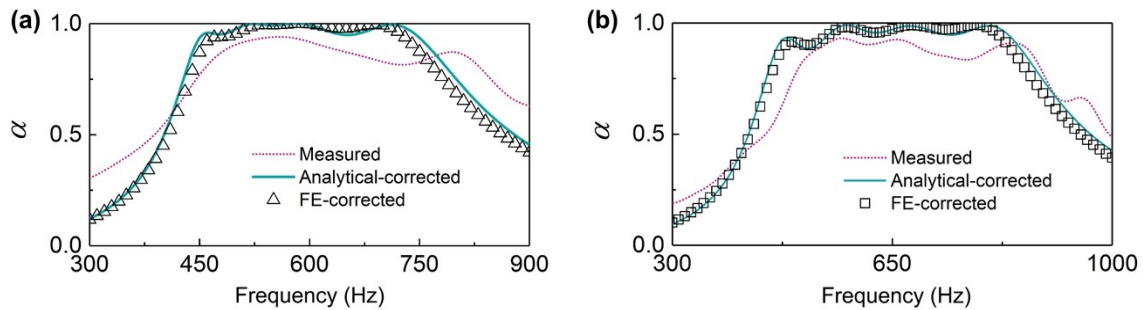


Figure S4. The calculations and FE results under corrected pore sizes of (a) Sample 1 and (b) Sample 2 compared with the measured data.

Section S2. Heterogeneity-based parallel design

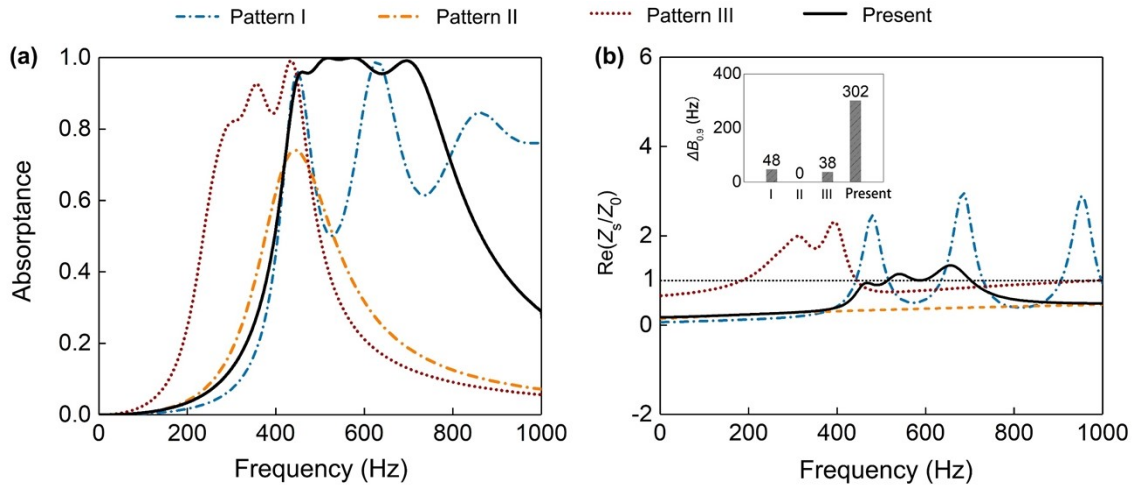


Fig. S5. Comparison between representative heterogeneous and homogeneous arrangements in terms of (a) absorptive performance, and (b) acoustic resistance and the bandwidth at $\alpha = 0.9$. The geometries of Pattern I-III are obtained by re-arranging the parameters of the present one (Table S5).

Table S5. Acoustic parameters of the compared patterns in Fig. S5. (Unit: mm).

Parameters	L_c	t_{plate}	d_i	σ_i	D
Pattern I	12.00	2.00	1.40	1.07%	48.00
			1.40	2.14%	
			1.40	4.28%	
			1.40	8.55%	
Pattern II	12.00	2.00	1.40	1.07%	48.00
			1.40	1.07%	
			1.40	1.07%	
			1.40	1.07%	
Pattern III	12.00	2.00	1.40	1.07%	48.00
			1.10	0.66%	
			0.90	0.44%	
			0.80	0.35%	

Section S3. FE modelling

The FE model in COMSOL Multiphysics is shown in Fig. S6. The top layer is set as the perfectly matched layer to mimic non-reflecting infinite fields above the model domain meshed by swept meshing of triangular elements. Then is followed by the background pressure layer that generate

the incident acoustic pressure. The lower portion refers to the fluid both in the perforations and cavities. All these air domains are meshed by tetrahedral elements. For the improved accuracy, the mesh of perforations is sufficiently refined with the defaults as: minimum mesh size of 0.26 mm and curvature factor of 0.4.

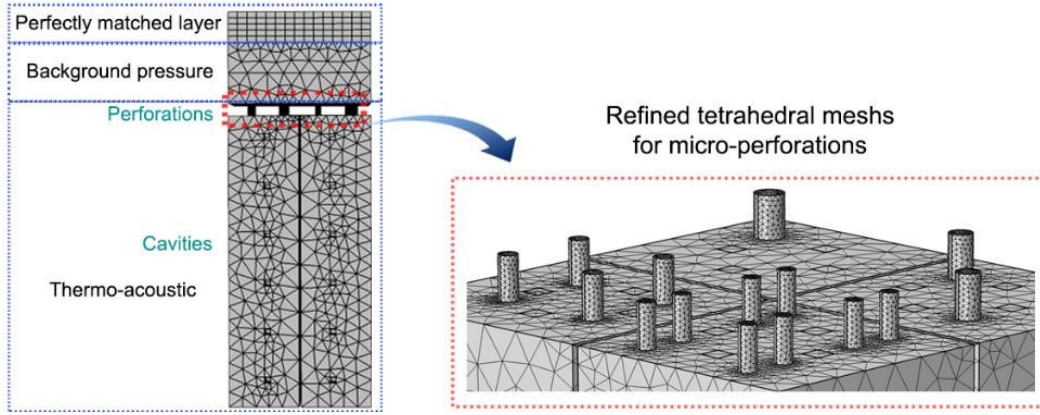


Fig. S6. The FE model of our metamaterials in COMSOL Multiphysics with meshed details shown.

Here are the equations embedded in Thermo-viscous Module in COMSOL.

$$i\omega\rho = -\rho_0(\nabla \cdot u) \quad (S1)$$

$$i\omega\rho_0u = \nabla \cdot \left(-pI + \mu\left(\mu_B - \frac{2}{3}\mu\right)(\nabla \cdot u)I \right) \quad (S2)$$

$$i\omega(\rho_0c_pT - T_0\alpha_0p) = -\nabla \cdot (-\tau\nabla T) \quad (S3)$$

where T and p refer to temperature and air pressure, respectively. μ_B represents the bulk viscosity. c_p , α_0 and τ represent specific heat at constant pressure, thermal expansion coefficient and thermal conductivity of air, respectively. u and I are the vibration velocity of the particle and the identity matrix.

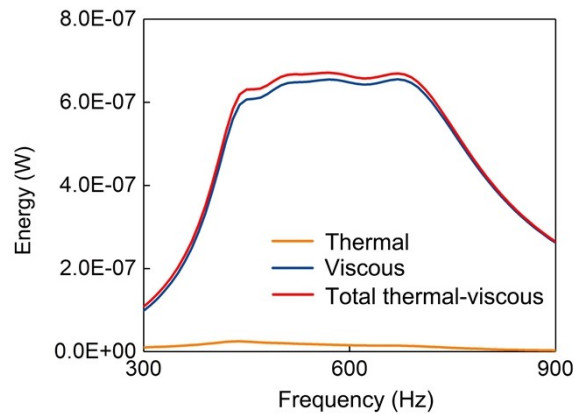


Fig. S7. Thermal, viscous, and total viscous-energy dissipation by all the pores and cavities in simulation.

Section S4. Physics underlying the excellent absorption

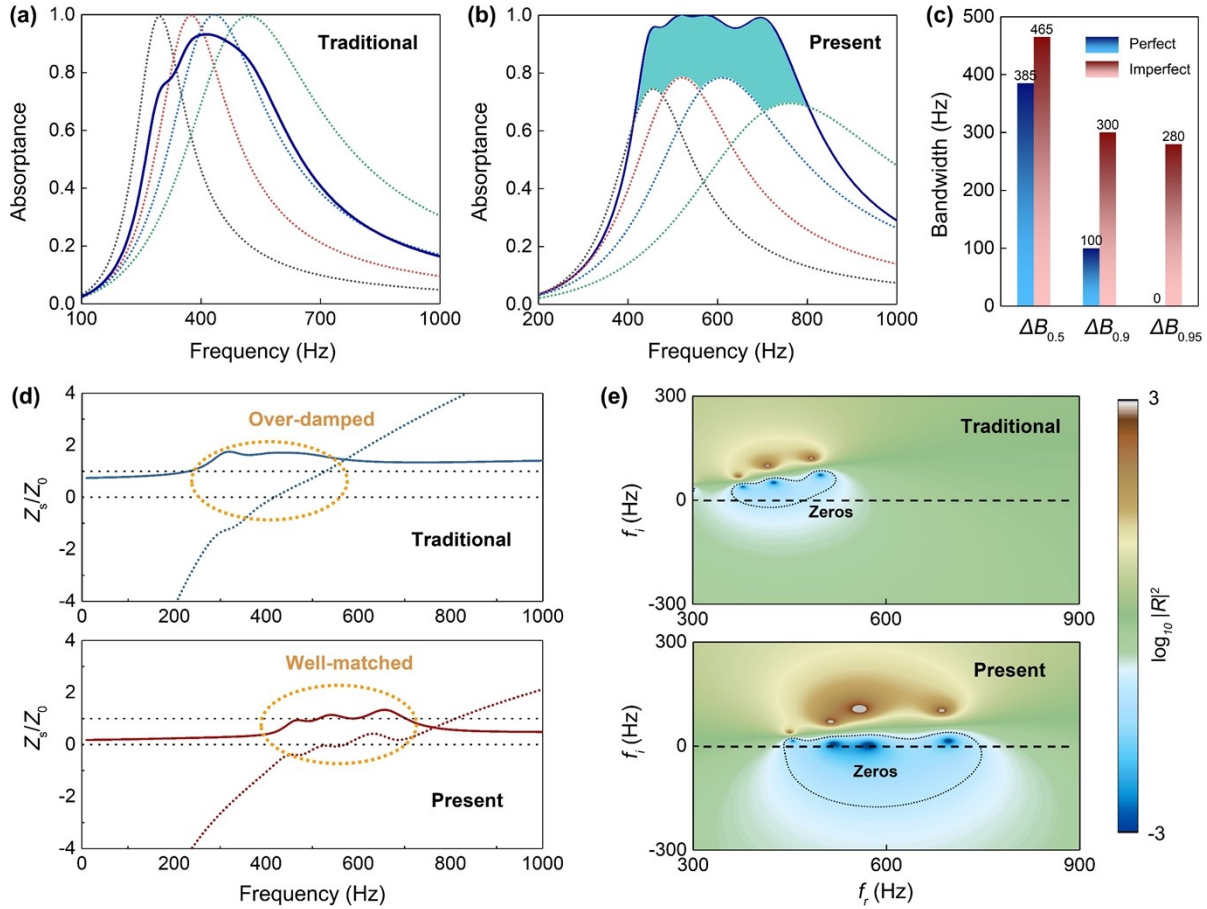


Fig. S8. Illustration of weak-resonance based design strategy. (a) Absorptive performance of DPMM with all components achieving perfect absorption. (b) Absorptive performance of DPMM with all components showing weaker absorption (0.6-0.8). (c) Comparison of bandwidth at $\alpha=0.5, 0.9$ and 0.95 of DPMM consisting of PCs and ICs. (d) Compared acoustic resistance and reactance when applying PCs and ICs. Arranging PCs leads to the over-damped condition, while the resistance gets well-matched for ICs case. (e) Representation of the reflection coefficient in the complex frequency plane of when applying PCs and ICs. The dotted contour lines are plotted to demonstrate the quasi-perfect absorption domains where $a > 0.9$.

Fig. S9 depicts how to facilitate the damping state balance in a low-frequency broadband regime in this work. Focusing on the target domain, the above discussed weak-resonances are obtained

via lower individual damping state. Emerging from optics, this highly efficient approach attracts increasing concerns in the past two years⁶⁻¹⁰. This tailored system breaks the limitation of damping manipulation compared to traditional recipes.

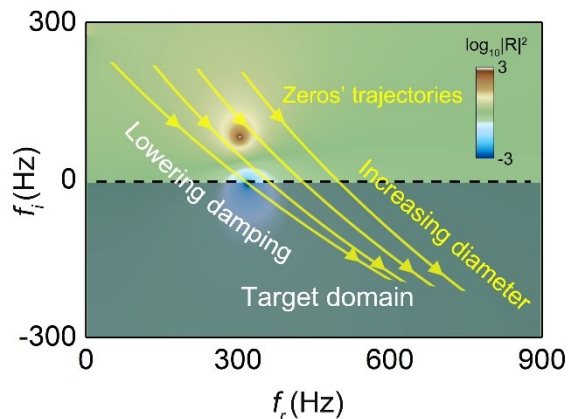


Fig. S9. Representation of the reflection coefficient of dexterously tuned ICs in the complex frequency plane.

Section S5. Cyclic compressive performance

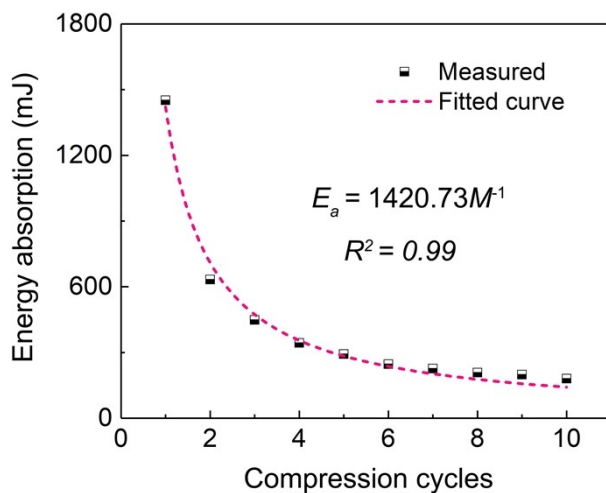


Fig. S10. Energy absorption performance of each compression cycle with the fitted curve displayed.

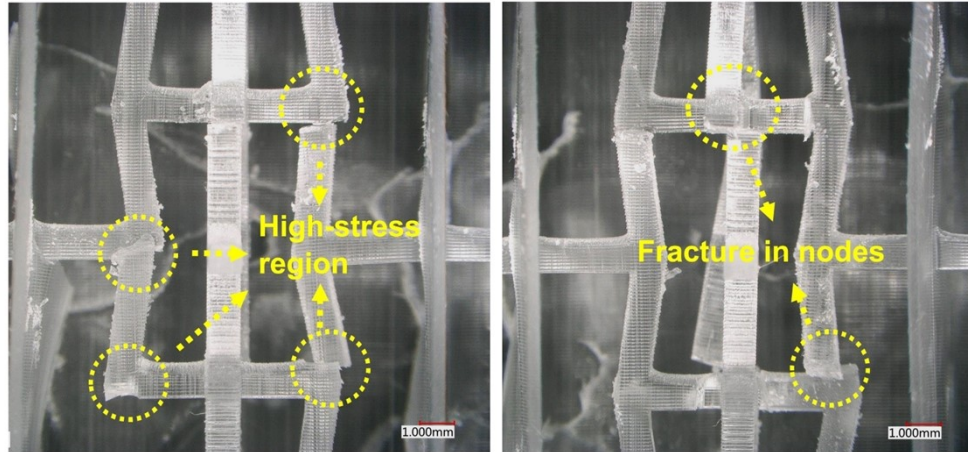


Fig. S11. Fracture details of DPMM specimens. The fracture is always occurred in the strut's nodes.

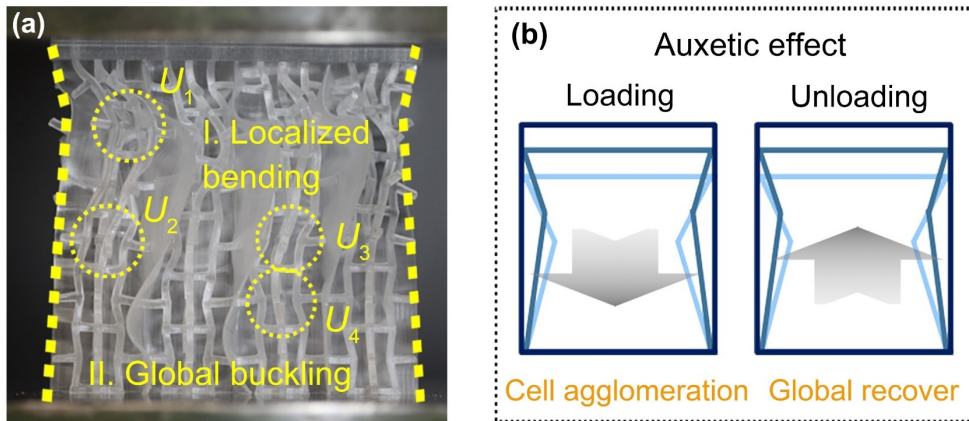


Fig. S12. Deformation mechanism. (a) Deformation mode when $\varepsilon = 0.1$. Representative buckling re-entrant units are circled. The bending of localized units contributes to the global buckling. (b) Macroscopic deformation mode in the cases of loading and unloading.

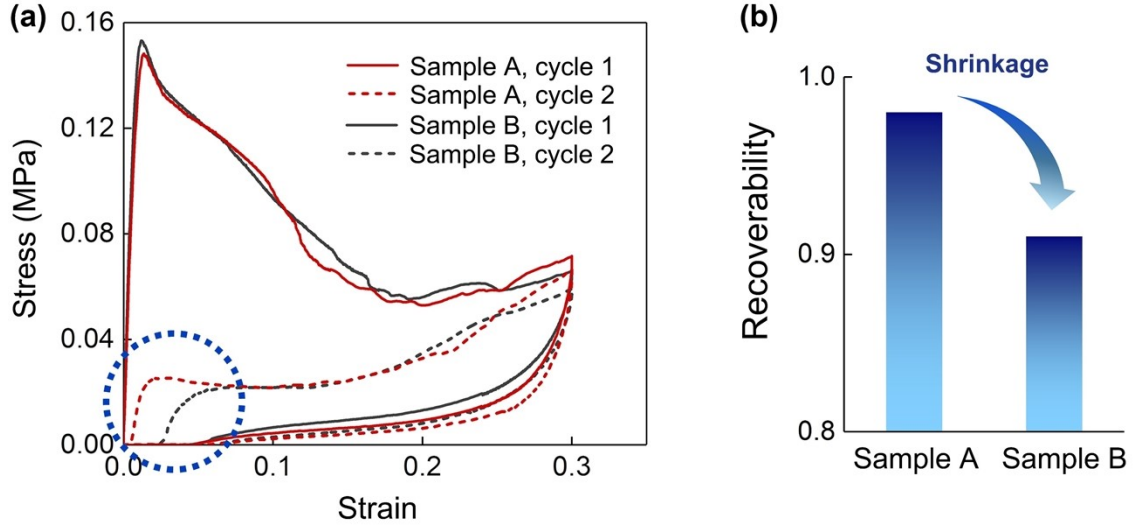


Fig. S13. Observation of viscoelastic effect by experimental comparisons. (a) Viscoelastic effect characterized by comparing the stress-strain curves of Sample A (with 300 s relaxed time) and Sample B (without relaxed time). (b) Shrinkage of recoverability.

Section S6. Demonstration of tunability

Table S6 presents the geometric parameters for on-demand sound absorption in Fig. 5(a)-(b). Particularly, for an extremely-low frequency absorption, an embedded hollow tube is added under the perforation, and its wall thickness is 400 μm with height of 46 mm. The left 2 mm space in cavity is remained for air flowing. Other models are all fundamental micro-perforated panels.

Table S6. Acoustic parameters in the cases given in Fig. 5(a)-(b) (Unit: mm).

	Performance	L_c	t_{plate}	n_i	d_i	D
A specific frequency	Extremely-low	48.00	2.00	1	5.00	48.00
	Medium	24.00	2.00	1	1.40	48.00
	Low	12.00	2.00	1	1.00	48.00
A broad frequency	Low	24.00	2.00	1	2.20	48.00
				2	1.70	
				4	1.40	
	Medium	12.00	2.00	6	1.35	48.00
				1	1.60	
				2	1.30	
High	6.00	2.00	6	0.95	24.00	
			12	0.90		

3	0.80
9	0.60
20	0.55

Fig. S14 depicts the introduced double-arrowhead and SC-sphere lattice. Corresponding deformations mode and damage characteristics are marked in the figure. Geometries of arrowhead and SC-based metamaterials in Fig. 5 are given here. In Fig. 5(c)-(d), for arrowhead type, $L_a = 12$ mm, $t_a = 1.4$ mm, $l_a = 1.57$ mm, $\theta_{a1} = 27^\circ$, and $\theta_{a2} = 17^\circ$. For SC-based type, $R_s = 4$ mm, $t_s = 2$ mm and $L_s = 12$ mm. In Fig. 5(e)-(g), when the units are doubled, for re-entrant type, $L_r = 4.22$ mm; $H_r = 5.6$ mm; $\theta_r = 81^\circ$; $t_r = 0.8$ mm; for arrowhead type: $L_a = 6$ mm, $t_a = 0.9$ mm, $l_a = 0.72$ mm, and θ_{a1} and θ_{a2} stay unchanged; for SC-based type, $R_s = 2$ mm, $t_s = 1$ mm and $L_s = 6$ mm.

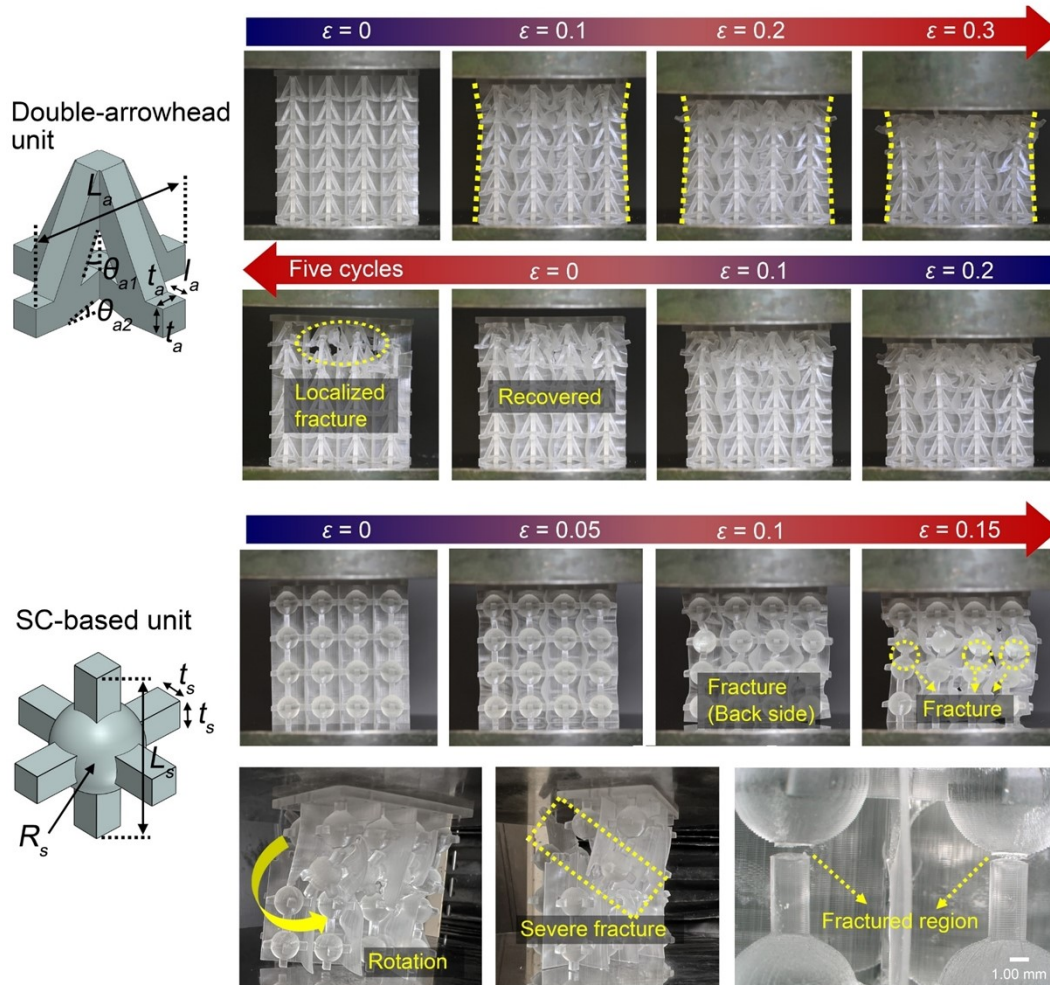


Fig. S14. Geometries of double-arrowhead and SC-based lattice units and corresponding deformation modes.

Fig. S15 shows the free-fall dropping tests process. The distance from dropping items to the objects (i.e., DPMM specimen and floor) is maintained as the same for each dropping case. For beaker, bulb, and goose eggs, the drop height is respectively set as 1.5 m, 1.5m, and 0.15 m.

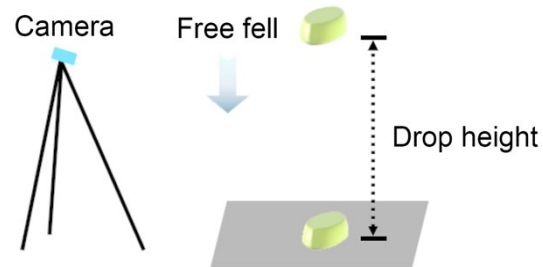


Fig. S15. Schematic of freely dropping tests when hitting on DPMM specimen and floor.

Video S1: Cushioning effect of DPMM

Section S6. Summary of superior mechanical and acoustic metamaterials.

Table S7 compares our metamaterials with the mainstream acoustic and mechanical metamaterials in terms of six criteria. The data are from the referenced literatures in main text. We compare these metamaterials carefully with available data and then score them reasonably as far as possible.

Table S7. Comparison with superior mechanical and acoustic metamaterials.

	Low-frequency absorption	Continuous broadband	Resilience	Safety		Designability	Practicality		
Advanced absorbers	Minimum resonant frequencies: at 350 and 460 Hz ⁴ at 320 Hz ¹² (10/10)	Continuous excellent absorption spectra: from 350 to 460 Hz ⁴ from 320 to 6.4 kHz ¹² (10/10)	Plastics with horizontal walls—uncapable of recovering (0/10)	Processing	Strength (MPa)	High design freedom of impedance-related geometries (7/10)	Low-frequency absorption	Safety	Reusability
				FFF, FDM, LCD, DLP, etc.	NA ^a		High	High	Low
				(8/10)			(7/10)		
Advanced foams	Minimum resonant frequencies: around 500 Hz ¹³ around 1500 Hz ¹⁴ (7/10)	Continuous excellent absorption spectra: from 500 to 6.3 kHz ¹³ from 1.0 to 6.0 kHz ¹⁴ (10/10)	Fully recoverable ¹³ NA ¹⁴ (10/10)	Hazardous precursors; synthetic fibers	NA	Limited design freedom (3/10)	Medium	Low	High
				(5/10)			(7/10)		
Microlattice metamaterials	Minimum resonant frequencies: > 1000 Hz ^{15,16} ; NA ¹⁷ (3/10)	Obvious absorption valleys from 1.0 -6.0 kHz ^{15,16} NA ¹⁷ (5/10)	Uncapable of recovering ^{15,16} Recoverability close to 1.0 ¹⁷ (6/10)	Metal powders (20 – 100 μm) ^{15,16}	> 30 ¹⁵ > 100 ¹⁶ < 1.0 ¹⁷	High design freedom of materials and geometries, etc. (9/10)	Low	Medium	Medium
				Template-based ¹⁷	(6/10)		(6/10)		
This work	Minimum resonant frequencies: at 458 Hz (9/10)	Continuous excellent absorption spectra: 458 Hz to 834 Hz (9/10)	High recoverability up to 98% (9/10)	DLP-3D printing	< 1.0	High design freedom of both acoustic and mechanical units (9/10)	High	High	High
				(9/10)			(9/10)		

^a NA: Not applicable or not available.

References.

1. Zhou, Z., Huang, S., Li, D., Zhu, J. & Li, Y. Broadband impedance modulation via non-local acoustic metamaterials. *Natl Sci Rev* (2021) doi:10.1093/nsr/nwab171.
2. Ma, F., Wang, C., Du, Y., Zhu, Z. & Wu, J. H. Enhancing of broadband sound absorption through soft matter. *Mater Horiz* (2022) doi:10.1039/d1mh01685g.
3. Guo, J., Zhang, X., Fang, Y. & Jiang, Z. A compact low-frequency sound-absorbing metasurface constructed by resonator with embedded spiral neck. *Appl Phys Lett* **117**, (2020).
4. Wu, F. *et al.* Low-frequency sound absorption of hybrid absorber based on micro-perforated panel and coiled-up channels. *Appl Phys Lett* **114**, (2019).
5. Xu, W., Liu, J., Yu, D. & Wen, J. Coherent coupling based meta-structures for high acoustic absorption at 220–500 Hz frequency. *Applied Acoustics* **182**, (2021).
6. Wang, Z., Guo, Z., Li, Z. & Zeng, K. Coupling and scaling effect for low-frequency broadband sound absorption via vertex-based hierarchy. *Appl Phys Lett* **119**, (2021).
7. Roca, D. & Hussein, M. I. Broadband and Intense Sound Transmission Loss by a Coupled-Resonance Acoustic Metamaterial. *Phys Rev Appl* **16**, (2021).
8. Huang, S. *et al.* Compact broadband acoustic sink with coherently coupled weak resonances. *Sci Bull (Beijing)* **65**, (2020).
9. Chen, A. *et al.* Machine learning-Assisted low-frequency and broadband sound absorber with coherently coupled weak resonances. *Appl Phys Lett* **120**, (2022).
10. Duan, M., Yu, C., Xin, F. & Lu, T. J. Tunable underwater acoustic metamaterials via quasi-Helmholtz resonance: From low-frequency to ultra-broadband. *Appl Phys Lett* **118**, (2021).
11. Ren, X., Shen, J., Tran, P., Ngo, T. D. & Xie, Y. M. Design and characterisation of a tuneable 3D buckling-induced auxetic metamaterial. *Mater Des* **139**, (2018).
12. Zhou, Z., Huang, S., Li, D., Zhu, J. & Li, Y. Broadband impedance modulation via non-local acoustic metamaterials. *Natl Sci Rev* (2021) doi:10.1093/nsr/nwab171.
13. Zong, D. *et al.* Bubble Templated Flexible Ceramic Nanofiber Aerogels with Cascaded Resonant Cavities for High-Temperature Noise Absorption. *ACS Nano* (2022) doi:10.1021/acsnano.2c06011.
14. Pang, K. *et al.* Highly Efficient Cellular Acoustic Absorber of Graphene Ultrathin Drums. *Advanced Materials* **34**, (2022).
15. Li, Z. *et al.* Additively manufactured dual-functional metamaterials with customisable mechanical and sound-absorbing properties. *Virtual Phys Prototyp* **17**, 864–880 (2022).
16. Li, X. *et al.* Microlattice Metamaterials with Simultaneous Superior Acoustic and Mechanical Energy Absorption. *Small* **17**, (2021).
17. Schaedler, T. A. *et al.* Ultralight metallic microlattices. *Science (1979)* **334**, (2011).